

A human brain atlas of χ -separation for normative iron and myelin distributions

Kyeongseon Min¹, Beomseok Sohn², Woo Jung Kim^{3,4}, Chae Jung Park⁵, Soohwa Song⁶, Dong Hoon Shin⁶, Kyung Won Chang⁷, Na-Young Shin⁸, Minjun Kim¹, Hyeong-Geol Shin^{9,10}, Phil Hyu Lee¹¹, Jongho Lee^{1,*}

¹Department of Electrical and Computer Engineering, Seoul National University, Seoul, Republic of Korea

²Department of Radiology, Samsung Medical Center, Sungkyunkwan University School of Medicine, Seoul, Republic of Korea

³Institute of Behavioral Sciences in Medicine, Yonsei University College of Medicine, Seoul, Republic of Korea.

⁴Department of Psychiatry, Yongin Severance Hospital, Yonsei University College of Medicine, Yongin, Republic of Korea.

⁵Department of Radiology, Yongin Severance Hospital, Yonsei University College of Medicine, Yongin, Republic of Korea

⁶Heuron Co., Ltd, Republic of Korea

⁷Department of Neurosurgery, Severance Hospital, Yonsei University College of Medicine, Seoul, Republic of Korea

⁸Department of Radiology, Severance Hospital, Yonsei University College of Medicine, Seoul, Republic of Korea

⁹Department of Radiology, Johns Hopkins University School of Medicine, Baltimore, MD, USA

¹⁰F.M. Kirby Research Center for Functional Brain Imaging, Kennedy Krieger Institute, Baltimore, MD, USA

¹¹Department of Neurology, Severance Hospital, Yonsei University College of Medicine, Seoul, Republic of Korea

*Correspondence: jonghoylee@snu.ac.kr

Abstract

Iron and myelin are primary susceptibility sources in the human brain. These substances are essential for healthy brain, and their abnormalities are often related to various neurological disorders. Recently, an advanced susceptibility mapping technique, which is referred to as χ -separation (pronounced as “chi”-separation), has been proposed, successfully disentangling paramagnetic iron from diamagnetic myelin. This method opened a potential for generating high resolution iron and myelin maps in the brain. Utilizing this technique, this study constructs a normative χ -separation atlas from 106 healthy human brains. The resulting atlas provides detailed anatomical structures associated with the distributions of iron and myelin, clearly delineating subcortical nuclei, thalamic nuclei, and white matter fiber bundles. Additionally, susceptibility values in a number of regions of interest are reported along with age-dependent changes. This atlas may have direct applications such as localization of subcortical structures for deep brain stimulation or high-intensity focused ultrasound and also serve as a valuable resource for future research.

Keywords: susceptibility source separation, *chi*-separation atlas, *x*-separation atlas, quantitative susceptibility mapping, iron imaging, myelin imaging

Abbreviations: DBS, deep brain stimulation; DTI, diffusion tensor imaging; HIFU, high-intensity focused ultrasound; MPRAGE, magnetization-prepared rapid gradient echo; MWF, myelin water fraction; MWI, myelin water imaging; QSM, quantitative susceptibility mapping; SWI, susceptibility-weighted imaging

Word counts: 7424 words

1. Introduction

In the human brain, iron and myelin are essential components for normal brain functions¹. Alterations in iron deposition or demyelination are often observed in neurodegenerative diseases such as multiple sclerosis, Parkinson's disease, and Alzheimer's disease¹, making iron and myelin as potential biomarkers for these diseases. Therefore, *in-vivo* imaging techniques capable of mapping iron and myelin distributions may have significant clinical value.

Magnetic resonance imaging (MRI) has been shown to be a potential tool that reveals iron and myelin distributions *in vivo*. For example, iron has been imaged using techniques such as relaxometry (R_2^2 ; R_2^* and $R_2'^3$), susceptibility-weighted imaging (SWI)⁴, and quantitative susceptibility map (QSM)⁵. Similarly, myelin has been visualized using magnetization transfer⁶, R_1 maps⁷, myelin water imaging (MWI)⁸, and QSM. Among these techniques, QSM is shown to be sensitive to both iron and myelin and provides quantitative measurements⁹⁻¹².

Because QSM maps reflect the superposition of magnetic susceptibility sources, however, QSM encounters a limitation in distinguishing the contribution of iron and myelin. In particular, when iron and myelin are co-localized in a voxel, they result in the cancellation of paramagnetic iron and diamagnetic myelin contribution. To overcome this limitation, a susceptibility source separation method, which is referred to as χ -separation, was recently proposed¹³. This method jointly utilizes phase and R_2' (or R_2^*) to provide paramagnetic susceptibility (χ_{para}) and diamagnetic susceptibility (χ_{dia}) maps. Studies have demonstrated strong correlations between χ_{para} and iron, and between χ_{dia} and myelin, suggesting potential use of the two maps as surrogate biomarkers for iron and myelin¹⁴⁻¹⁶. Furthermore, this approach has been suggested to provide potentially meaningful information when evaluating neurological disorders such as multiple sclerosis and neuromyelitis optica spectrum disorder^{13,17-20}. Alternative methodologies and technical developments have been continued, expanding future applications of the susceptibility source separation field²¹⁻²³.

In neuroimaging, a brain atlas serves as a common reference, facilitating comprehensive analysis of brain images acquired from diverse population and modalities, and has been widely utilized for investigating stereotactic anatomical features, conducting longitudinal studies, enabling automatic parcellation, and identifying neuropathological alterations²⁴. With a novel MR image contrast, a corresponding atlas has been created to support and promote its utilization in research. Specifically, for iron and myelin imaging, QSM atlases²⁵⁻²⁷, and MWI atlases^{28,29} have been developed and utilized in various applications^{26,29}. Recently, a susceptibility source separation atlas has also become available³⁰, which employed APART-QSM technique²³ to separate susceptibility sources.

In this study, our objective is to establish a normative χ -separation atlas of the healthy human brain. Our atlas aims to visualize detailed anatomical structures related to iron and myelin distributions, and provide normal values of paramagnetic and diamagnetic susceptibility in anatomical regions.

The atlas may be useful in clinical applications for deep brain stimulation (DBS) or high-intensity focused ultrasound (HIFU) by localizing subcortical nuclei. Additionally, the atlas may help us to identify susceptibility alterations associated with neurodegenerative diseases. The χ -separation atlas, along with regions of interest (ROI) labels, regional susceptibility values, and demographic data are made publicly available (<https://github.com/SNU-LIST/chi-separation-atlas>).

2. Methods

2.1. Subjects

A total of 116 healthy human volunteers aged 27–85 years (interquartile range: 47.5–76.5, median: 65, mean: 62.1 ± 15.8 ; 37 males and 79 females) were recruited from two centers (Yonsei Severance Hospital (YSSH) and Yongin Severance Hospital (YGSH)). The inclusion criteria are detailed in Supplementary Information. All subjects provided written informed consent. The study was reviewed and approved by the Institutional Review Board. After reviewing datasets, nine subjects were excluded due to severe calcification in globus pallidus, and one subject was excluded due to motion artifacts. Consequently, the study population was reduced to 106 volunteers aged 27–85 years (interquartile range: 46–75, median: 64, mean: 60.8 ± 15.8 ; 34 males and 72 females).

2.2. MRI acquisition

The volunteers were scanned using one of two 3 T MRI scanners (Ingenia CX in YSSH or Ingenia Elition X in YGSH, Philips Healthcare) with 32-channel receiver head coils. T_1 -weighted and multi-echo GRE images were acquired for atlas construction. For the T_1 -weighted images, a 3D magnetization-prepared rapid gradient echo (MPRAGE) sequence was utilized with acquisition parameters summarized in Supplementary Information. For the 3D multi-echo GRE, images were acquired using a monopolar gradient readout with the following scan parameters: TR = 33 ms, TE = 5.25, 11.08, 16.91, 22.74, and 28.57 ms, flip angle = 15° , resolution = $1 \times 1 \times 1 \text{ mm}^3$, FOV = $256 \times 256 \times 144 \text{ mm}^3$, pixel bandwidth = 228 Hz, and SENSE acceleration factor = 2. The imaging orientations of both sequences were aligned with the anterior commissure-posterior commissure line.

2.3. χ -separation atlas construction

The workflow for the χ -separation atlas is depicted in Fig. 1. First, the T_1 -weighted image underwent B_1 bias field correction using a nonparametric nonuniform normalization algorithm³¹ (*N4BiasFieldCorrection*, ANTs, <https://github.com/ANTsX/ANTs>). Subsequently, a brain mask was obtained by applying a template-based brain extraction algorithm (*antsBrainExtraction.sh*, ANTs) to the bias field-corrected T_1 -weighted image.

The magnitude images of all echoes in the multi-echo GRE data were averaged and corrected for a B_1 bias field (*N4BiasFieldCorrection*, ANTs), generating a combined GRE image. Then, the T_1 -weighted image was registered to this image using an affine transformation with six degrees of freedom (*antsRegistration*, ANTs). The brain mask from the T_1 -weighted image was also transformed to the multi-echo GRE space using the affine transformation.

To generate a χ -separation map, a processing pipeline established in the χ -separation toolbox (<https://github.com/SNU-LIST/chi-separation>) was employed. The χ -separation model and its implementation were reported previously^{13,32}. Briefly, it is based on a biophysical model that describes the contributions of paramagnetic susceptibility (χ_{para}) and diamagnetic susceptibility (χ_{dia}) to the magnetic field perturbation (Δf) and the reversible transverse relaxation rate ($R_2' = R_2^* - R_2$). The relationship is expressed as follows¹³:

$$\Delta f = D_f * (\chi_{para} + \chi_{dia}) \quad (1)$$

$$R_2' = D_{r,para} |\chi_{para}| + D_{r,dia} |\chi_{dia}| \quad (2)$$

where D_f is the dipole kernel, and $D_{r,para}$ and $D_{r,dia}$ are the relaxometric constants relating R_2' to the paramagnetic and diamagnetic susceptibility, respectively. In our study, a neural network implementation of χ -separation which is called χ -sepnet- R_2^* was employed³² (<https://github.com/SNU-LIST/chi-separation>). This neural network was trained using multi-head orientation data as labels to provide streaking artifact-free χ_{para} and χ_{dia} maps³³. Additionally, the network was trained to use R_2^* instead of R_2' as the input data, allowing the creation of χ_{para} and χ_{dia} without R_2 . The outcome of this network has demonstrated a good agreement with that using R_2' input both in healthy volunteers³² and multiple sclerosis patients³⁴ at the cost of slight degradation in accuracy.

The inputs for χ -sepnet- R_2^* , which were a tissue field map (Δf) and an R_2^* map, were obtained from the multi-echo GRE data via the following steps. First, the phase maps from the multi-echo GRE data were unwrapped using the Laplacian-based unwrapping algorithm³⁵ (*MRPhaseUnwrap*, STI Suite, <https://people.eecs.berkeley.edu/~chunlei.liu/software.html>). The unwrapped phase maps were averaged using SNR-weighted mean³⁶ to produce a combined phase map. Then, the brain mask was applied. The result was processed to remove background field by applying V-SHARP³⁷ (STI Suite), generating a tissue field map (Δf). An R_2^* map was generated by fitting a mono-exponential decay function to the multi-echo magnitude signals using a nonlinear least square solver (*lsqnonlin*, MATLAB 2016b). Finally, Δf and R_2^* maps were applied to χ -sepnet- R_2^* ³² (*chi_sepnet_general*, *chi-separation* toolbox), creating χ_{para} and χ_{dia} maps. These two maps were summed to produce a QSM map.

This QSM map was linearly combined with the T_1 -weighted image, creating a hybrid image in order to achieve accurate registration of subcortical structures^{26,38,39}. Before the combination, the histogram of a T_1 -weighted image was normalized by a piecewise linear transformation that maps the deciles of the image to the averaged deciles of all T_1 -weighted images⁴⁰. The intensity-normalized T_1 -weighted image was scaled to the range of 0–255. Then the hybrid image was calculated as follows³⁹:

$$[\text{Hybrid image}] = [\text{Corrected } T_1\text{-weighted image}] - 0.8 (\text{ppb}^{-1}) \times [\text{QSM map (in ppb)}]. \quad (3)$$

This hybrid image was registered to the hybrid image atlas in the MNI space from MuSus-100³⁹, using a symmetric diffeomorphic image normalization algorithm⁴¹ (*antsRegistration*, ANTs). Subsequently, the χ_{para} and χ_{dia} maps were transformed to the MNI space using the same deformation field. The χ_{para} and χ_{dia} maps in the MNI space from the 106 subjects were averaged, creating χ_{para} and χ_{dia} atlases. Similarly, QSM, hybrid, and T_1 -weighted image atlases were created by averaging these images in the MNI space. To evaluate the subject-dependent variability of the atlases, a voxel-wise relative standard deviation (*rSD*) was calculated, creating the *rSD* maps of χ_{para} and χ_{dia} .

$$[rSD \text{ of a voxel}] (\%) = [\text{Standard deviation of all subjects}] / | [\text{Mean of all subjects}] | \times 100. \quad (4)$$

2.4. Atlas analysis

To explore the characteristics of the χ -separation atlas, regions of interest (ROIs) were selected in subcortical nuclei, thalamic nuclei, and white matter fiber bundles. For the subcortical and thalamic nuclei, parcellation labels from MuSus-100 atlas were employed. Thalamic nuclei ROIs in MuSus-100 were manually refined into four ROIs: medial thalamic nuclei, lateral thalamic nuclei, pulvinar, and whole thalamus. For white matter, the T_1 -weighted image atlas with white matter labels from ICBM-DTI-81⁴² was registered to our T_1 -weighted image atlas. Then, the white matter labels were eroded with a radius of 1 mm to reduce registration errors, defining white matter ROIs. Out of twenty-eight ROIs, the largest thirteen ROIs were selected, discarding small ROIs with large registration errors. Additionally, a whole white matter mask, generated from the hybrid images via tissue segmentation⁴³, was included as white matter ROI. Consequently, eight subcortical nuclei, four thalamic nuclei, and fourteen white matter ROIs were employed (Fig. S1). Prior to the ROI analysis, the intersection of the subcortical nuclei, thalamic nuclei, and white matter ROIs was excluded to ensure that they were mutually exclusive. Then, median χ_{para} , χ_{dia} , and QSM values were extracted from the ROIs. Median was used instead of mean to enhance statistical robustness against outlier voxels such as vessels and calcification within the ROIs. The median values were averaged across subjects to report the population means and standard deviations.

The population-averaged χ_{para} and QSM values in the five subcortical nucleus ROIs were linearly regressed with respect to the non-heme iron content from literature⁴⁴ to demonstrate the well-known linear relationship^{9,25,45}. The R^2 value, regression line and its 95% confidence interval were calculated and the significance of the regression coefficients was assessed using *t*-tests.

To examine the relationship of χ_{dia} and myelin content, a myelin water fraction (MWF) atlas²⁸ was employed as a surrogate marker for myelin content. Before the analysis, the T_1 -weighted image atlas (ICBM-152) accompanied with the MWF atlas were registered to our T_1 -weighted image atlas, and then the MWF atlas was transformed using the same deformation field. The χ_{dia} values in the white matter ROIs were linearly regressed with respect to the MWF values in the same ROIs. The R^2 value, regression line, and its 95% confidence interval were calculated and the significance of the regression coefficients was assessed. To account for the errors in both χ_{dia} and MWF values, Deming regression was performed to fit the observations to a regression line.

Lastly, age-dependent iron and myelin changes were explored for each ROI. The individual median values of χ_{para} and χ_{dia} in each ROI were linearly regressed against age. The R^2 value, the regression line, and its 95% confidence interval were calculated and the significance of the regression coefficients was assessed using *t*-tests. The significance level was Bonferroni-corrected, considering the total number of ROIs, which was 26.

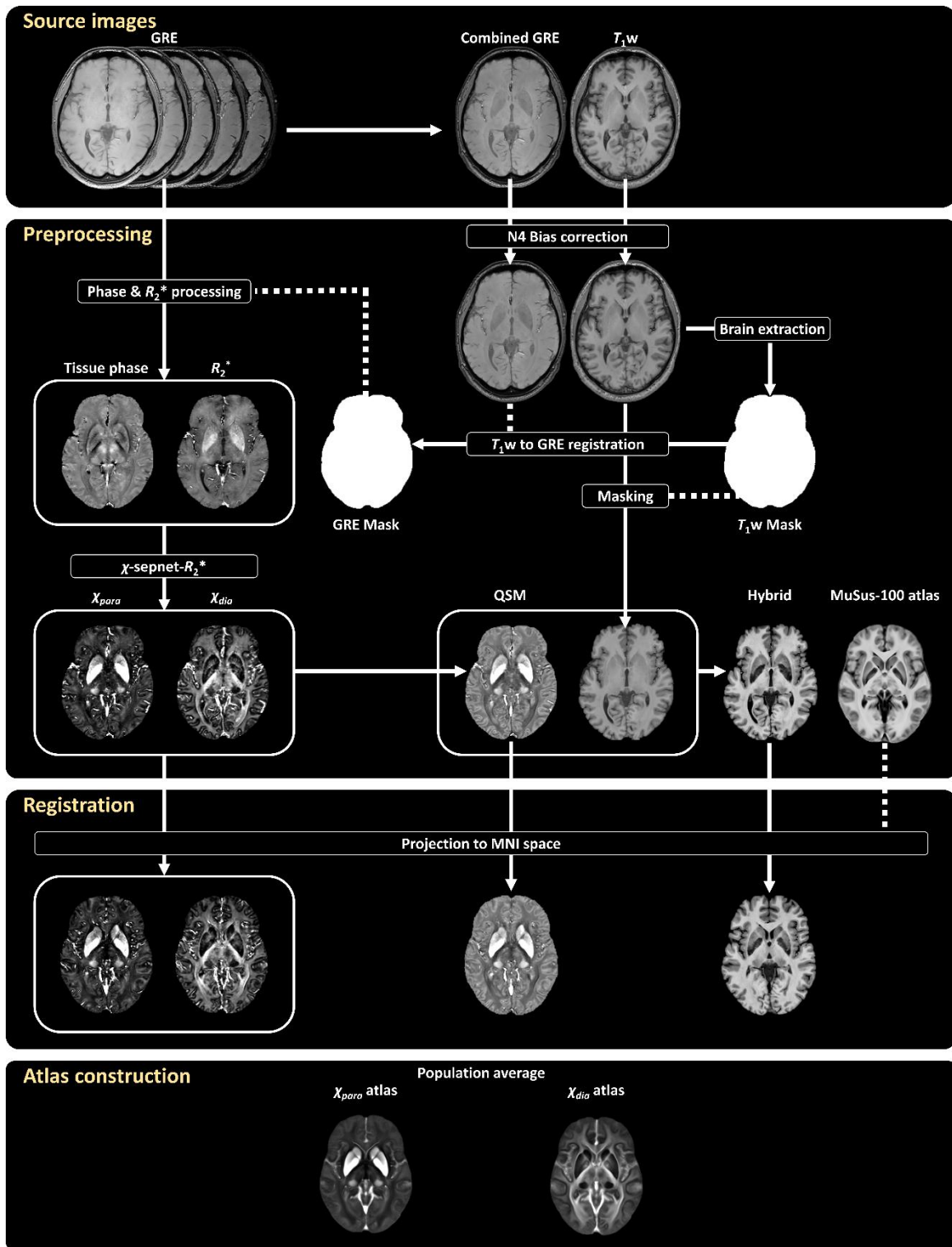


Fig. 1. Schematic flowchart illustrating the processing pipeline for generating the χ_{para} and χ_{dia} atlases. The hybrid images were created by a linear combination of the QSM and T_1 -weighted images to improve registration in the deep gray matter area.

3. Results

3.1. χ_{para} and χ_{dia} atlases

Figure 2 shows representative slices in the axial, coronal and sagittal planes of the population-averaged χ_{para} and χ_{dia} atlases and corresponding rSD maps. The χ_{para} atlas highlights regions rich in iron, such as caudate nucleus, putamen, globus pallidus, pulvinar, subthalamic nucleus, red nucleus, substantia nigra, and ventral pallidum, which exhibit high χ_{para} values. On the other hands, white matter structures reveal high $|\chi_{dia}|$ values in corpus callosum, external capsule, internal capsule, optic radiation, optic tract, cingulum, fornix, and cerebellar peduncle. It should be noted that artifacts, mostly from large vessels, exist in both atlases (see Discussion and Fig. S2). The rSD maps have high values in regions with low susceptibility and/or regions close to large vessels and ventricles.

In Fig. 3, ten axial slices of the χ_{para} and χ_{dia} atlases that contain distinctive susceptibility distributions are displayed. Regions not covered in Fig. 2, such as the dentate nucleus (DN, $z = -38$ mm), corticospinal tract (CST, $z = -30$ mm), pontine crossing tract (PCT, $z = -30$ mm), and hand knob of primary motor cortex (M1, $z = +55$ mm), are visible in the axial slices. Overall, the χ_{para} and χ_{dia} atlases provide detailed anatomical information that reflects well-known distributions of iron and myelin in the brain.

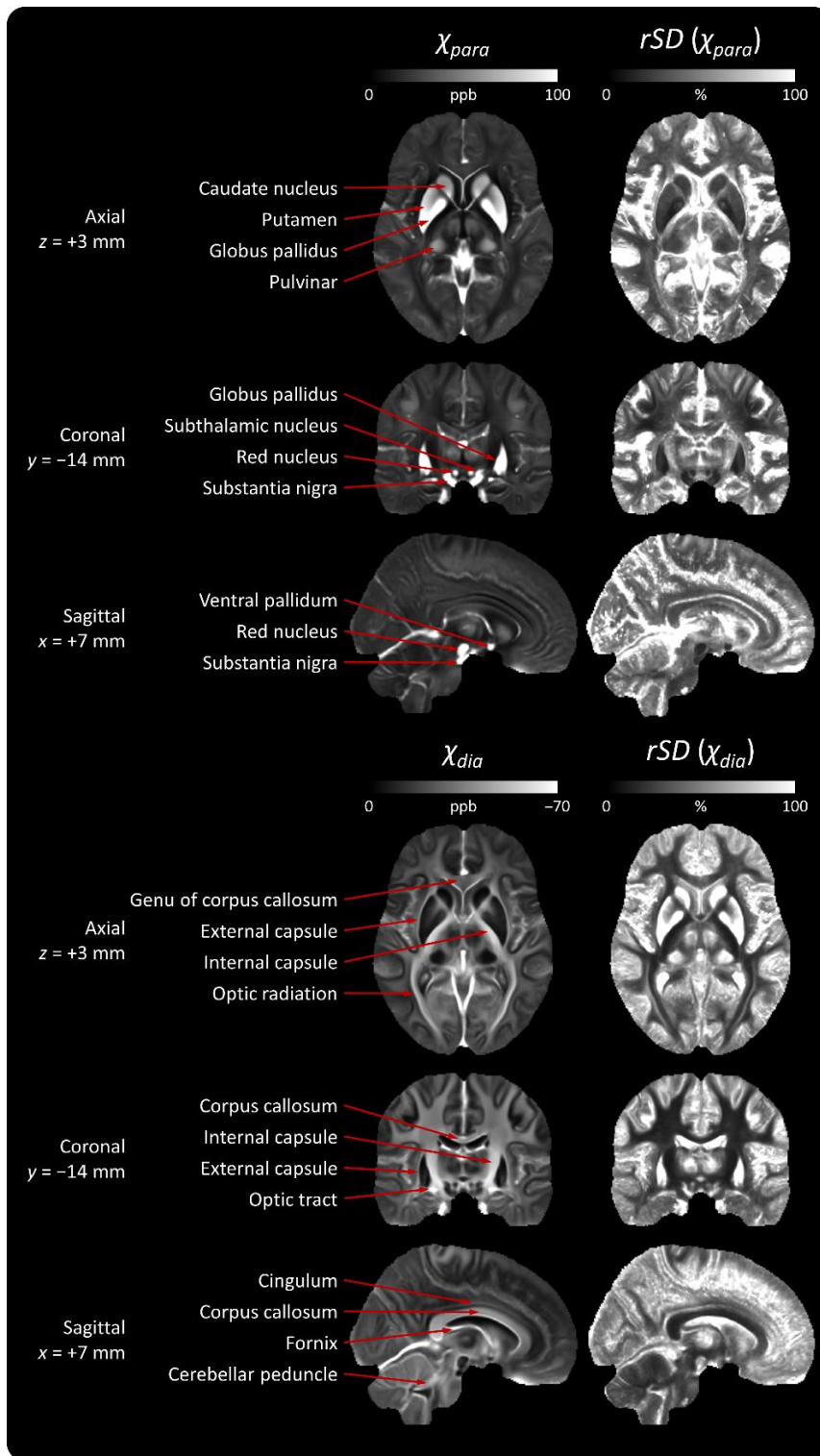


Fig. 2. Representative axial, coronal, and sagittal slices of the χ_{para} and χ_{dia} atlases and rSD maps.

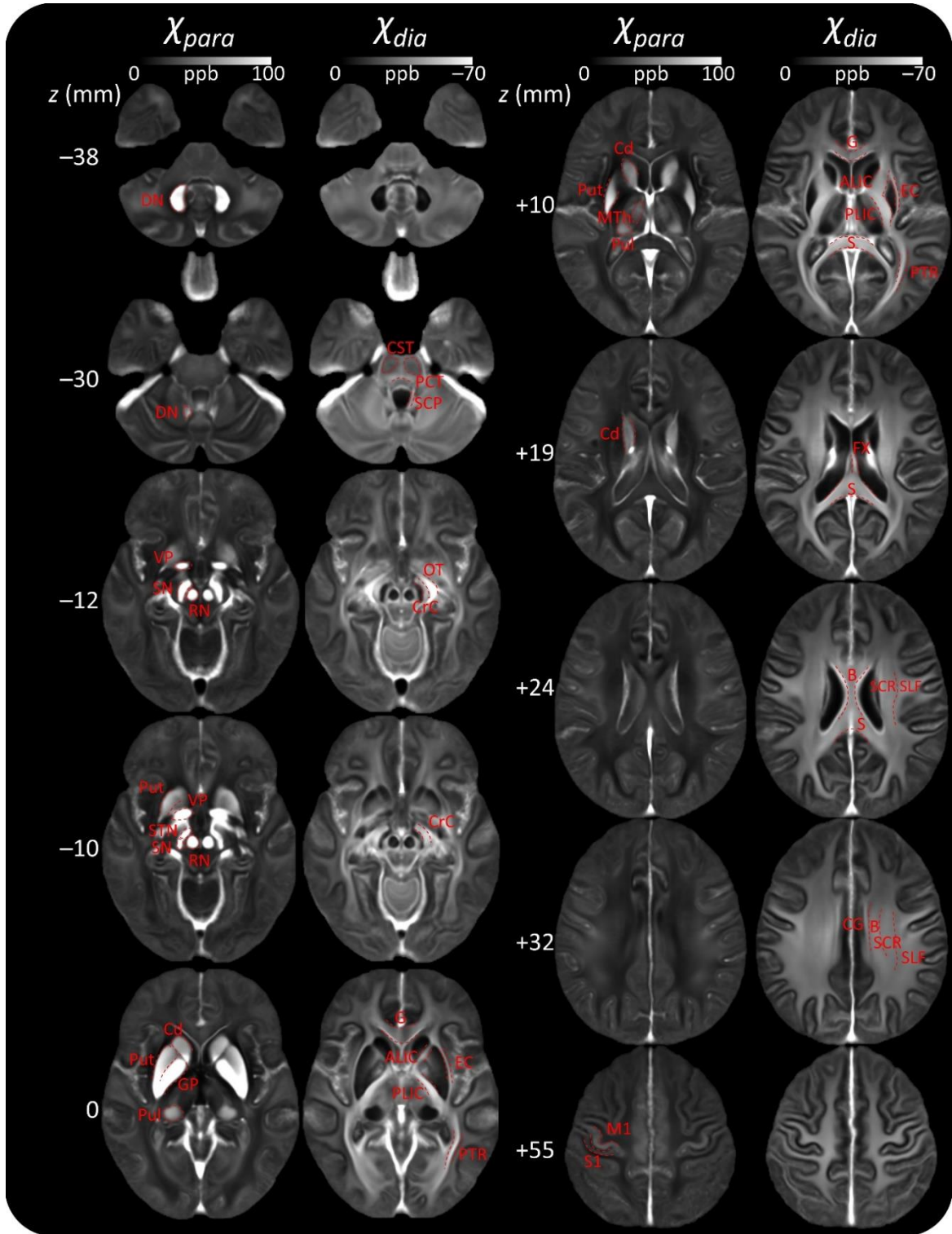


Fig. 3. Ten axial slices of the χ_{para} and χ_{dia} atlases. Anatomical structures are marked with red dotted lines. [DN: dentate nucleus, SN: substantia nucleus, VP: ventral pallidum, RN: red nucleus, Put: Putamen, STN: subthalamic nucleus, Cd: caudate nucleus; GP: globus pallidus, Pul: pulvinar, MTh: medial thalamic nuclei group, PCT: pontine crossing tract, CST: corticospinal tract, SCP: superior cerebellar peduncle, OT: optic tract, CrC: crus cerebri, ALIC: anterior limb of internal capsule, PLIC: posterior limb of internal capsule, EC: external capsule, PTR: posterior thalamic radiation, G: genu of corpus callosum, B: body of corpus callosum, S: splenium of corpus callosum, FX: fornix, CG: cingulum, SCR: superior corona radiata, SLF: superior longitudinal fasciculus, M1: primary motor cortex, S1: primary somatosensory cortex]

3.2. Details of anatomical structures

When basal ganglia and midbrain areas are examined, they reveal exquisite details of anatomy (Fig. 4). The zoomed-in images of the yellow rectangles are presented next to histology images from the literatures (Perls' stain images from⁴⁶; Heidenhain-Woelcke's stain images from⁴⁷). The iron distribution in the stained images, which are stained in cyan (darker color means more iron), is qualitatively well-delineated in the χ_{para} maps, revealing fine structures like claustrum (Cl, upper row), anterior (A)/medial (M)/lateral (L) thalamic nuclei groups (middle row), and external (GPe) and internal (GPi) globus pallidus (bottom row). Some of these structures may not be easily identified in other MRI images. The χ_{dia} maps reflect myelin distribution in the myelin stained images (darker color means more myelin). For example, external capsule (EC, upper row), posterior limb of internal capsule (PLIC, middle row) and anterior limb of internal capsule (ALIC, lower row) demonstrate high concentrations of myelin while Cl, Put (all rows) and Cd (bottom row) are lacking myelin. In particular, lateral thalamic nucleus (L) possesses moderate concentrations of iron and myelin in the histology, which are also correctly-depicted in the χ -separation maps, supporting successful separation of the para- and diamagnetic susceptibility sources (middle row). In contrast, the other thalamic nuclei (A, M, and Pul) show high concentrations of iron with no or little sign of myelin while PLIC suggests the opposite characteristics. All of these observations are well-matched to the χ -separation results (middle row). Lastly, lateral medullary laminae (LML), which separates the putamen (Put) and external globus pallidus, and medial medullary laminae (MML), which separates the external and internal globus pallidus, are also observed (bottom row).

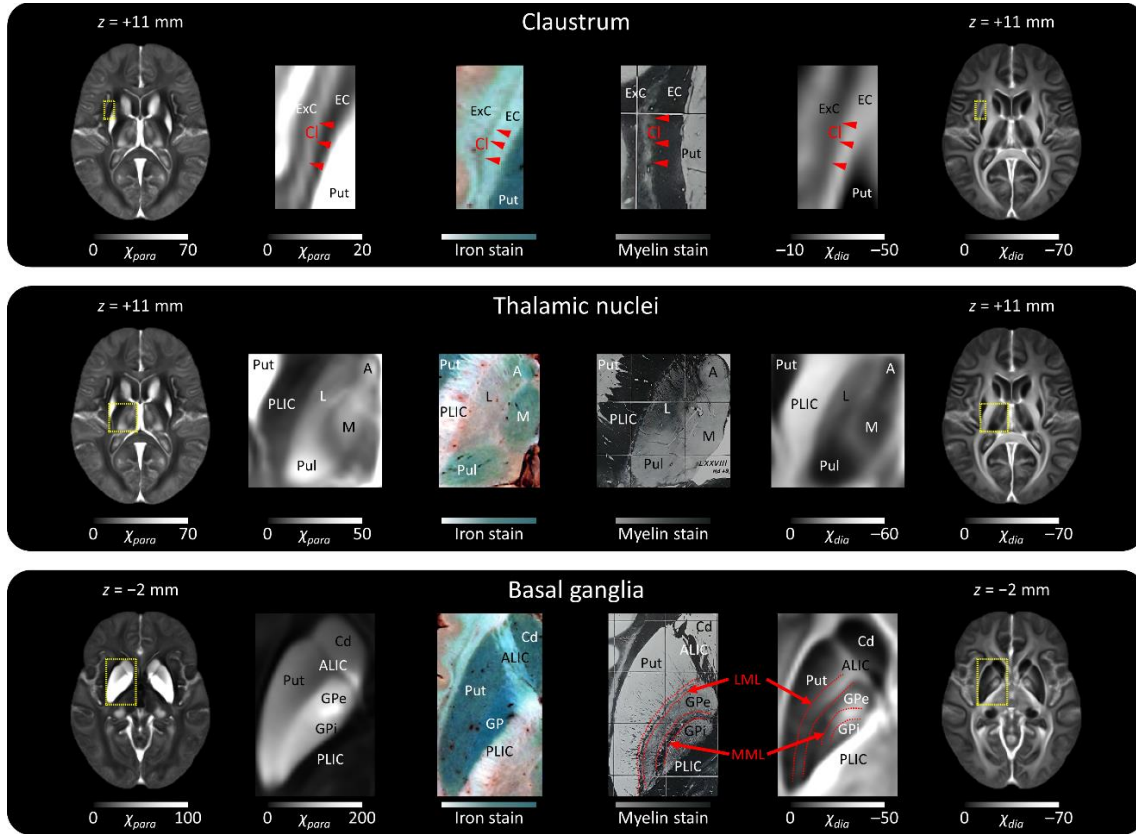


Fig. 4. Structures in the χ_{para} and χ_{dia} atlases presented along with the corresponding iron and myelin staining images. The zoomed-in images correspond to the regions indicated with yellow rectangles in the axial slices. The iron staining images are adapted and resized from Naidich et al.⁴⁶. The myelin staining images are adapted and resized from Schaltenbrand and Wahren⁴⁷. The claustrum (Cl), lateral (LML) and medial (MML) medullary lamina are marked with red arrows. [ExC: extreme capsule, EC: external capsule, Cl: claustrum, Put: Putamen, A: anterior thalamic nuclei group, M: medial thalamic nuclei group, L: lateral thalamic nuclei group, Pul: pulvinar, ALIC: anterior limb of internal capsule, PLIC: posterior limb of internal capsule, LML: lateral medullary lamina, MML: medial medullary lamina, Cd: caudate nucleus, GP: globus pallidus, GPe: external globus pallidus, GPi: internal globus pallidus]

3.3. ROI analysis

The means and standard deviations of χ_{para} , χ_{dia} , and QSM in the ROIs are plotted in Fig. 5 and summarized in Table S1. All the subcortical nuclei reveal high values of χ_{para} and much lower values of χ_{dia} , indicating predominant concentration of iron in the regions. The ventral pallidum ROI exhibits the highest χ_{para} value of 144.3 ± 27.0 ppb, followed by globus pallidus (131.9 ± 10.4 ppb), substantia nigra (115.7 ± 14.4 ppb), subthalamic nucleus (112.1 ± 12.1 ppb), red nucleus (112.0 ± 14.8 ppb), putamen (77.1 ± 20.6 ppb), and pulvinar (52.1 ± 11.6 ppb). In thalamus, the lateral thalamic nuclei ROI reports comparable levels of χ_{para} (22.0 ± 5.2 ppb) and χ_{dia} (-22.4 ± 4.7 ppb), which are in good agreement with the iron and myelin staining images in Fig. 4, demonstrating successful separation of para- and diamagnetic susceptibility. On the other hand, medial thalamic nuclei and pulvinar ROIs yield higher concentration of χ_{para} (medial thalamic nuclei = 31.2 ± 7.6 ppb and pulvinar = 52.1 ± 11.6 ppb) than χ_{dia} (medial thalamic nuclei = -11.8 ± 5.9 ppb and pulvinar = -4.4 ± 3.2 ppb). These measurements also qualitatively agree with the corresponding areas in the iron and myelin staining images of Fig. 4. In the white matter ROIs, $|\chi_{dia}|$ values are higher than χ_{para} values although a few ROIs (e.g., superior longitudinal fasciculus) report moderate values of χ_{para} . The posterior limb of internal capsule has the lowest χ_{dia} value of -52.2 ± 3.0 ppb (or the highest negative susceptibility). The second lowest χ_{dia} value is observed in the cerebral peduncle (-43.7 ± 4.1 ppb) followed by splenium of corpus callosum (-42.3 ± 3.1 ppb), anterior limb of internal capsule (-41.3 ± 4.0 ppb), and posterior thalamic radiation (-41.1 ± 4.0 ppb).

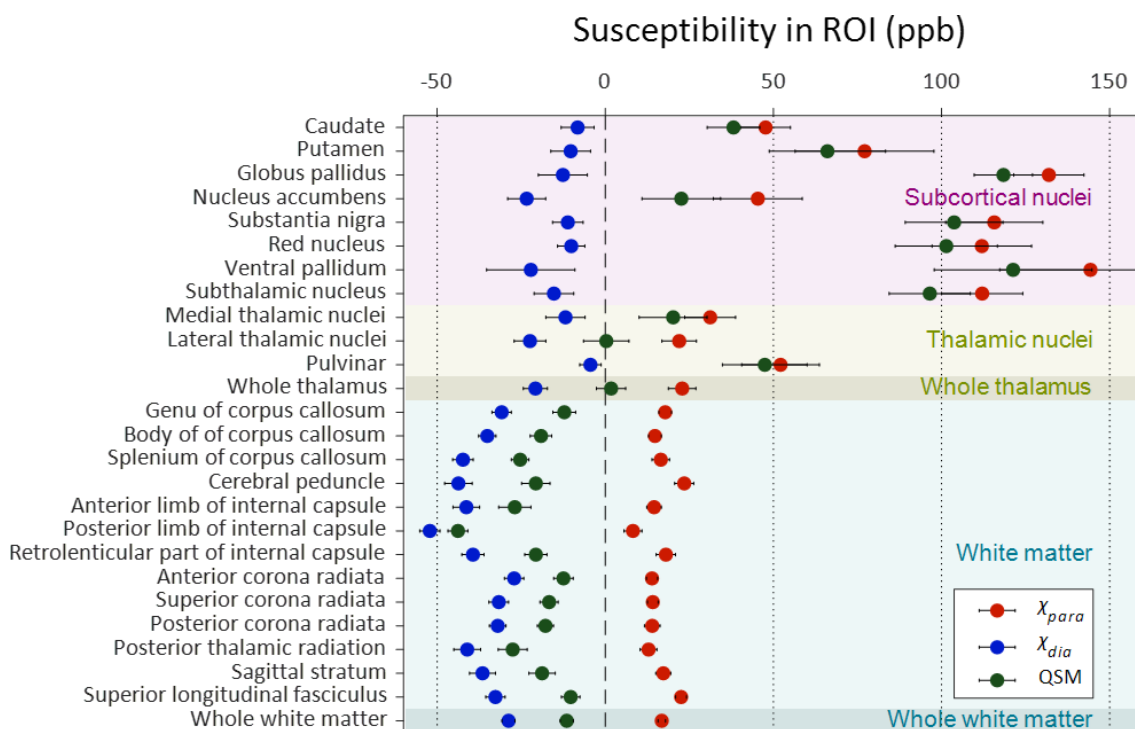


Fig. 5. The population averages of χ_{para} , χ_{dia} , and QSM medians extracted from 26 ROIs (number of subjects = 106). Red, blue, and green circles represent the χ_{para} , χ_{dia} , and QSM averages, respectively. The black line attached to the circle indicates the standard deviation value of each ROI.

When the χ_{para} ROI values are further inspected by plotting them against the postmortem iron content measurements⁴⁴, they report a clear linear trend ($R^2 = 0.99$, Fig. 6A). The linear regression line is:

$$\chi_{para} \text{ (ppb)} = 6.8 \times \text{iron content (mg/100 g)} - 15. \quad (5)$$

While the linear coefficient is statistically significant ($p < 0.001$), the intercept is not ($p = 0.15$).

Likewise, when the QSM values are linearly regressed with the iron content, a similar linear trend is observed ($R^2 = 0.99$, Fig. 6B), consistent with the previous QSM studies^{25,45}. The regression line is:

$$\text{QSM (ppb)} = 6.6 \times \text{iron content (mg/100 g)} - 22. \quad (6)$$

Here, both the linear coefficient ($p < 0.001$) and the intercept ($p < 0.05$) are statistically significant. This intercept value, which is only significant in the QSM result, demonstrates that a non-zero offset exists between the iron and QSM relationship. This offset, potentially from diamagnetic susceptibility sources, is removed in χ_{para} results, reporting a reduced offset (statistically nonsignificant), suggesting that χ_{para} measurements better reflects iron than those of QSM.

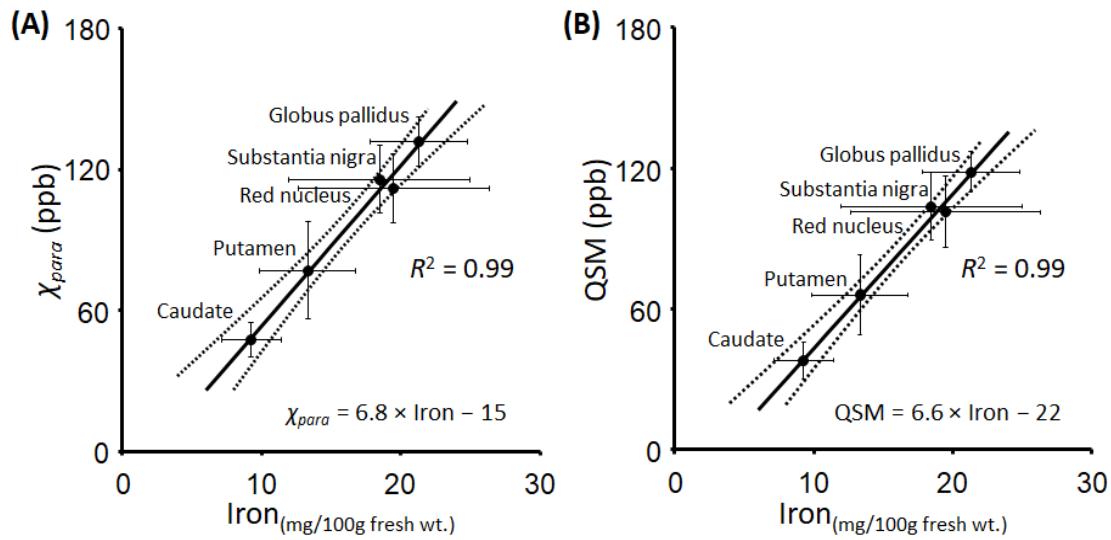


Fig. 6. Linear regression analysis between (A) χ_{para} or (B) QSM and iron content from the literature⁴⁴. The regression line is drawn with a solid line along with dotted lines representing 95% confidence intervals.

The χ_{dia} atlas and MWF atlas are visually compared in Fig. 7A. Overall, the χ_{dia} and MWF atlases show high values in myelin-rich structures such as posterior limb of internal capsule, posterior thalamic radiation, and splenium of corpus callosum, demonstrating a notable correspondence between the two atlases. Some areas (e.g. superior corona radiata), however, reveal differences potentially due to biases of the methods (e.g. fiber orientation effects). Figure 7B shows the results of linear regression analysis between the white matter ROI values of our χ_{dia} atlas and MWF atlas. The analysis shows a significant positive correlation ($R^2 = 0.71$). The linear regression line is:

$$|\chi_{dia}| \text{ (ppb)} = 3.6 \times \text{MWF (\%)} - 3.3. \quad (7)$$

The linear coefficient is statistically significant ($p < 0.05$), but the intercept is not ($p = 0.57$).

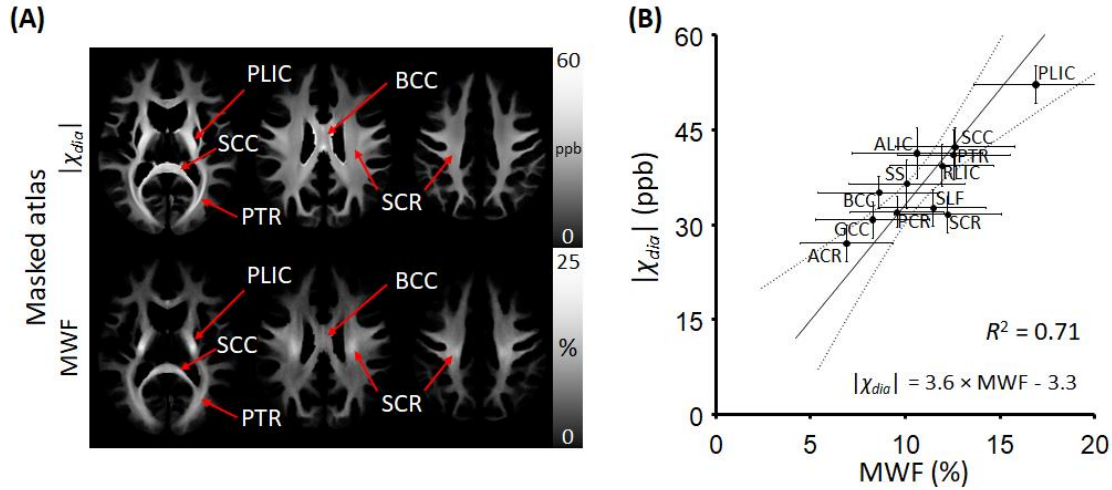


Fig. 7. The comparison between our χ_{dia} atlas and an MWF atlas from the literature²⁸. (A) A visual comparison of three representative slices of the χ_{dia} atlas and MWF atlas. The atlases are masked with the whole white matter ROI. (B) Linear regression analysis of the white matter ROIs values. The regression line is drawn with a solid line along with dotted lines representing 95% confidence intervals. [GCC: genu of corpus callosum, BCC: body of corpus callosum, SCC: splenium of corpus callosum, ALIC: anterior limb of internal capsule, PLIC: posterior limb of internal capsule, RLIC: retrolenticular part of internal capsule, ACR: anterior corona radiata, SCR: superior corona radiata, PCR: posterior corona radiata, PTR: posterior thalamic radiation, SS: sagittal striatum, SLF: superior longitudinal fasciculus]

3.4. Age-dependence of χ_{para} and χ_{dia}

The age-dependent susceptibility changes in the subcortical and thalamic nuclei ROIs are summarized in Fig. 8 (Table S2 for the statistics of linear regression). Putamen and nucleus accumbens (Fig. 8B, D) show significantly increasing trends in χ_{para} (putamen, $p = 1.6 \times 10^{-12}$; nucleus accumbens, $p = 1.8 \times 10^{-15}$; Bonferroni-corrected), whereas thalamus (Fig. 8L) shows a significantly decreasing trend (whole thalamus, $p = 1.7 \times 10^{-7}$; Bonferroni-corrected). Similar decreases are observed in medial thalamic nuclei ($p = 2.1 \times 10^{-4}$) and lateral thalamic nuclei ($p = 7.2 \times 10^{-7}$). The trends of putamen and thalamus are consistent with the age-dependent iron deposition reported in the literature⁴⁴. Caudate, globus pallidus, substantia nigra, red nucleus, ventral pallidum, and subthalamic nucleus show slightly positive slopes with no statistically significance. For $|\chi_{dia}|$, statistically significant increases are observed in caudate, putamen, globus pallidus, nucleus accumbens, and ventral pallidum whereas no significant changes were observed in the other ROIs.

Figure 9 shows the age-dependent susceptibility analysis in the white matter ROIs (Table S2 for the statistics of linear regression). Overall, white matter ROIs show decreasing trends in $|\chi_{dia}|$, with the whole white matter ROI revealing a significant decrease over the age range ($p = 2.7 \times 10^{-3}$, Bonferroni-corrected). This trend agrees with the previous studies using myelin water imaging⁴⁸⁻⁵⁰, suggesting a decrease of myelin with age. For χ_{para} , statistically significant decreases are observed in a few white matter ROIs while the other ROIs show almost no change.

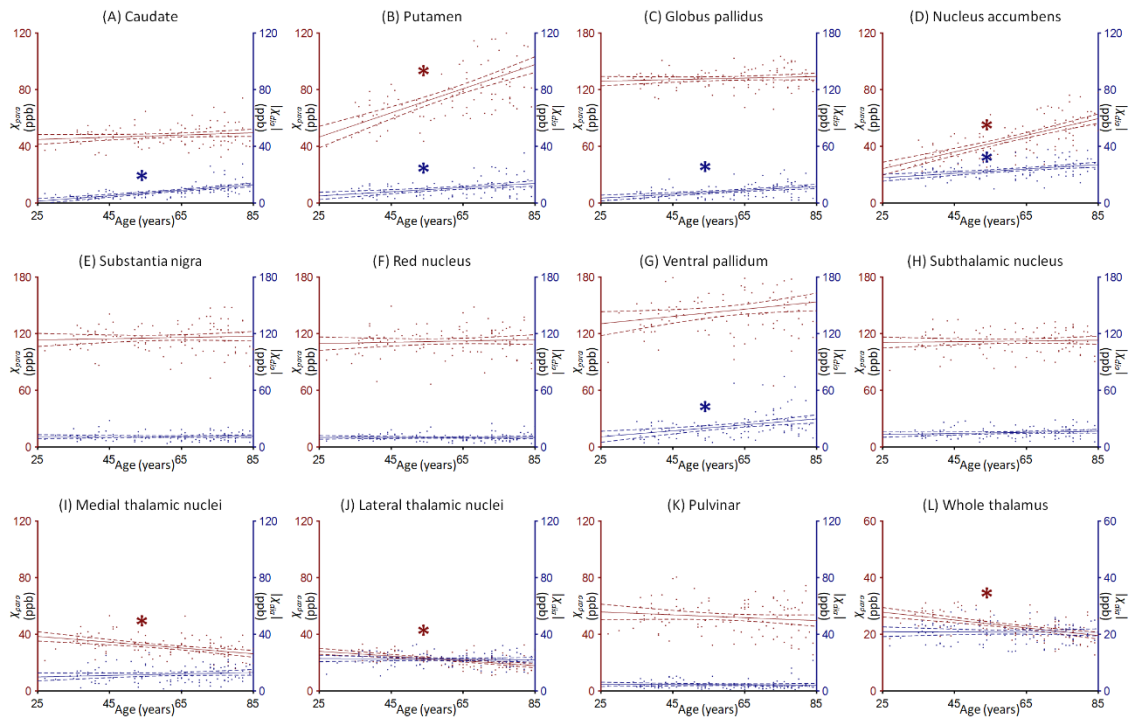


Fig. 8. The age-dependence of the χ_{para} and χ_{dia} values in the subcortical and thalamic nuclei ROIs: (A) Caudate, (B) putamen, (C) globus pallidus, (D) nucleus accumbens, (E) substantia nigra, (F) red nucleus, (G) ventral pallidum, (H) subthalamic nucleus, (I) medial thalamic nuclei, (J) lateral thalamic nuclei, (K) pulvinar, and (L) whole thalamus. The ordinate axes, data points, regression lines, and significance markers for χ_{para} and χ_{dia} values are colored with red and blue, respectively. The regression line is drawn with a solid line along with dotted lines representing 95% confidence intervals. The significance of the regression slope is marked with an asterisk (*, $p < 0.05$, Bonferroni-corrected).

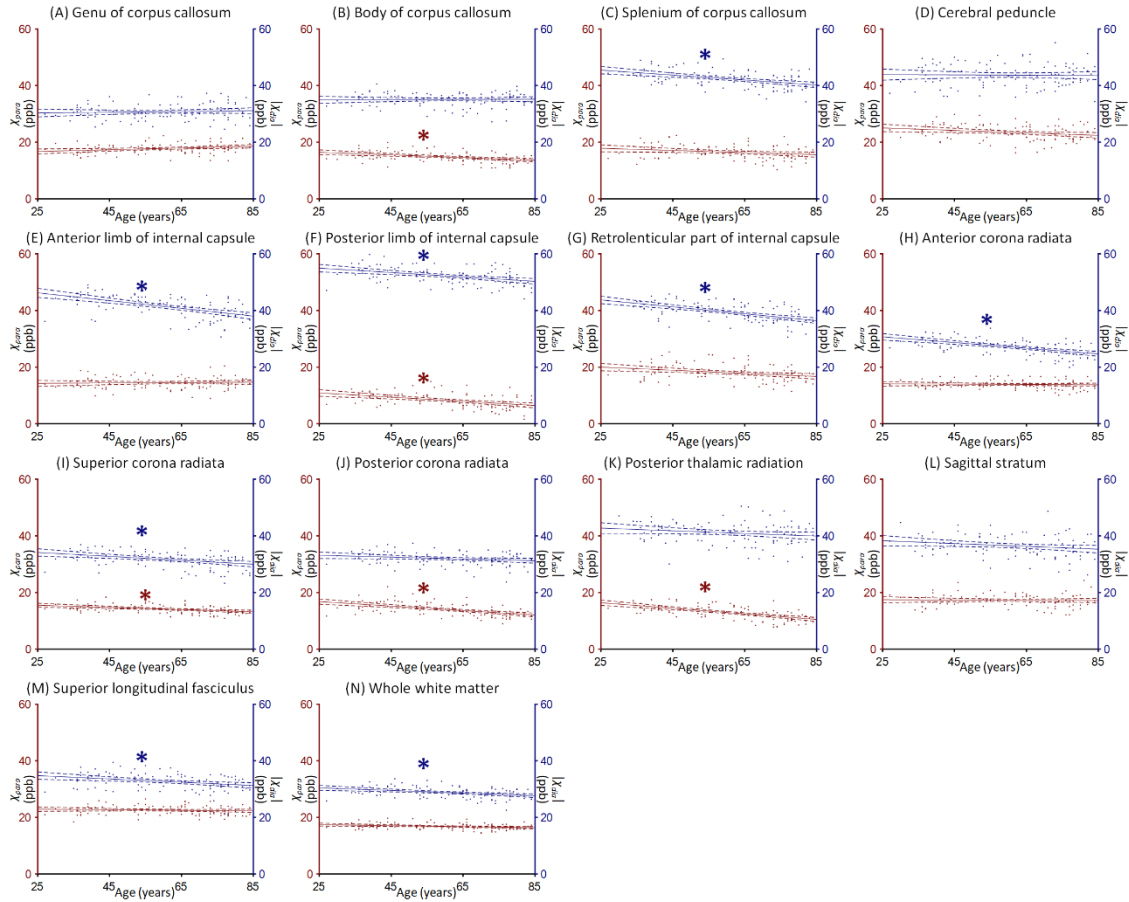


Fig. 9. The age-dependence of the χ_{para} and χ_{dia} values in the white matter ROIs: (A) Genu, (B) body, and (C) splenium of corpus callosum, (D) cerebral peduncle, (E) anterior limb, (F) posterior limb, and (G) retrolenticular part of internal capsule, (H) anterior, (I) superior, and (J) posterior corona radiata, (K) posterior thalamic radiation, (L) sagittal stratum, (M) superior longitudinal fasciculus, and (N) whole white matter. The ordinate axes, data points, regression lines, and significance markers for χ_{para} and χ_{dia} values are colored with red and blue, respectively. The regression line is drawn with a solid line along with dotted lines representing 95% confidence intervals. The significance of the regression slope is marked with an asterisk (*, $p < 0.05$, Bonferroni-corrected).

4. Discussion

In this study, we developed a χ -separation atlas for healthy population. Our atlas provides distributions of χ_{para} and χ_{dia} in the brain, successfully revealing details of subcortical nuclei, thalamic nuclei, and white matter fiber bundles.

The atlas may contain errors that have been identified in the previous χ -separation studies^{13,23}. The most notable source of errors is vessels in the brain (Fig. S2). Flow artifacts can hinder the accurate evaluation of tissue phase and R_2^* maps, leading to erroneous χ_{para} and χ_{dia} values. Additionally, vessels show large variability among subjects, creating unreliable regions with high rSD . Another major source of errors is anisotropy in the microstructure and susceptibility of myelin that may introduce fiber-orientation dependent variations in χ ^{51,52} and R_2^* ^{53,54}. This may introduce potentially higher χ_{dia} in perpendicular fibers than those in parallel fibers. The assumption of a constant D_r ($D_{r,para}$ and $D_{r,dia}$) across brain regions and among subjects may also introduce errors in the estimated susceptibility results, which will be a topic of continuing research^{23,55}.

The age distribution of our study spread over the range of 27–85 but the mean age of the population was 60.8 ± 15.8 years because the atlas is targeted toward population of neurodegenerative diseases. Therefore, caution should be exercised when applying our atlas to a young population (e.g., 20–30 years old). Considering the age-

dependence nature of iron accumulation⁴⁴ and myelination⁵⁶, another atlas is expected for the range of 0–30 years old that covers different characteristics of iron and myelin changes.

In our analysis, a linear function was fitted to explore age-dependent changes whereas a nonlinear trend was reported for non-heme iron accumulation over age [44]. We believe the linear fit is reasonable considering the study population (27–85 years old with the mean age of 60.8 years) because rapid iron accumulation occurs in the first two decades after birth whereas slower accumulation happens after the age of 30⁴⁴. Our results demonstrated significant iron accumulation over age in putamen, while caudate and globus pallidus did not reach statistical significance. This discrepancy may be due to iron accumulation slowing down earlier in globus pallidus and caudate than putamen⁴⁴. While some QSM studies have reported significant iron accumulation in globus pallidus and caudate^{57,58}, no significance was reported in other studies on older populations^{59,60}, potentially due to the difference in the age ranges of subjects. In some subcortical ROIs, $|\chi_{dia}|$ shows increasing trends with age, which are also reported in Lao et al.³⁰. The origin of these trends is unclear with no literature reporting myelin changes in these regions. In a DTI study, fractional anisotropy was reported to increase with age in putamen⁶¹, while another study found no significant change⁶². Further exploration is necessary to understand the source of this change.

In this study, many white matter ROIs revealed decreasing trends in $|\chi_{dia}|$ over age. For example, $|\chi_{dia}|$ decreased by 1.6%/decade in the whole white matter ROI. This finding is similar to age-dependent decrease in the MWF value in the whole white matter, which was approximately 1.4%/decade (calculated by the data points manually extracted between the ages of 30 and 79 from the work by Dvorak et al.²⁹). The negative linear trends of MWF with age have been demonstrated in other studies⁴⁸⁻⁵⁰ although quadratic trends were also suggested^{29,49,63}, which may be attributed to the white matter maturation in early adulthood⁵⁶. The difference in our trend may be from our older study population than the previous studies. In a few white matter ROIs, decreasing trends in χ_{para} were observed. Similarly, Lao et al.³⁰ reported decreasing χ_{para} after age of 40 in retrolenticular part of internal capsule. However, a postmortem iron assay study reported iron accumulation in cerebral white matter over lifespan⁶⁴, suggesting a need for further research to confirm the observation.

In contrast to a previous atlas study³⁰ utilizing APART-QSM technique²³, our study employed the χ -separation technique¹³ to generate the atlas. The two methods reported somewhat different ROI values: In particular, substantia nigra shows $\chi_{para} = 115.6$ ppb and $\chi_{dia} = -11.1$ ppb at the age of 60 in our study, whereas Lao et al.³⁰ reported approximately $\chi_{para} = 79$ ppb and $\chi_{dia} = -14$ ppb (based on the manually extracted data points from the regression lines at the age of 60). Considering the QSM value of substantia nigra from a meta-analysis (112.9 ± 37.7 ppb)⁶⁵, the sum of our χ_{para} and χ_{dia} values (= 104.5 ppb) show better agreement with the meta-analysis result than that of the previous study (= 65 ppb). Similar differences are also observed in other subcortical nuclei including red nucleus and globus pallidus. In addition to these differences, we aimed to conduct a comprehensive analysis and provide quantitative statistics for 26 ROIs from MuSus-100 and ICBM-DTI-81, covering a broader scope. The proposed atlas was further analyzed for iron and myelin distributions using staining images (Fig. 4), and χ_{para} correlated with iron content (Fig. 6) and χ_{dia} correlated with MWF (Fig. 7), further consolidating the relationship between χ_{para} vs. iron and χ_{dia} vs. myelin in a large population.

In a few subjects, large calcification was observed particularly in globus pallidus, reporting high $|\chi_{dia}|$ and χ_{para} potentially due to mineral deposition of diamagnetic calcium and paramagnetic iron⁶⁶. To avoid complications in the atlas, we excluded nine subjects with large calcification. Nevertheless, there were more subjects with small calcification that were not excluded, potentially introducing bias into the atlas. To mitigate this effect in the analysis, the median value was utilized instead of the mean value in the ROI analysis.

For the white matter ROIs, we utilized ICBM-DTI-81 atlas⁴², which is based on diffusion tensor imaging (DTI). However, we noticed that the χ_{dia} values exhibited pronounced heterogeneity within ROIs, suggesting that new ROIs need to be defined through the incorporation of DTI and myelin contents.

Beyond its application in research, our atlas may be utilized in intervention treatments, specifically in DBS and HIFU. Our atlas helps accurate localization of commonly stimulated targets in DBS, such as the internal globus pallidus and subthalamic nucleus⁶⁷. Similarly, for HIFU application, our atlas could facilitate the precise targeting of deep brain structures in the thalamus and basal ganglia⁶⁸, potentially improving the outcome of ablation.

5. Conclusion

In conclusion, our study successfully created a χ -separation atlas for healthy population, providing normative distributions of χ_{para} and χ_{dia} in the brain. The atlas offers insights into the spatial distributions of iron and myelin and allows us to delineate fine structures relevant to the susceptibility distributions. We expect that future research built upon our atlas will help to understand the spatial distributions of iron and myelin in the healthy human brain and their alterations in neurological disorders.

Acknowledgements

This research was supported by the National Research Foundation of Korea (2021R1A2B5B03002783, 2021M3E5D2A01024795, 2021R1I1A1A01040374, and 2022R1A4A1030579), INMC and IOER at Seoul National University and Heuron Co., Ltd. The ICBM-DTI-81 atlas was obtained as a courtesy of Dr. Mori (www.mristudio.org) in Johns Hopkins University. We thank for the kind permission to reproduce figures from other publications. The iron staining images in Fig. 4 were published in Naidich *et al.*, *Imaging of the Brain*, pp. 174-204, Copyright Elsevier (2013). The myelin staining images in Fig. 4 were published in Schaltenbrand & Wahren, *Atlas for Stereotaxy of the Human Brain*, Plates 51-55, Copyright Thieme (1977).

Data availability statement

The data and materials that support the findings and the conclusion of this study are made publicly available (<https://github.com/SNU-LIST/chi-separation-atlas>).

References

1. Möller HE, Bossoni L, Connor JR, et al. Iron, myelin, and the brain: Neuroimaging meets neurobiology. *Trends in Neurosciences*. 2019;42:384-401. doi:<https://doi.org/10.1016/j.tins.2019.03.009>
2. Drayer B, Burger P, Darwin R, Riederer S, Herfkens R, Johnson GA. Magnetic resonance imaging of brain iron. *Am J Neuroradiol*. 1986;7:373-380.
3. Ordidge RJ, Gorell JM, Deniau JC, Knight RA, Helpert JA. Assessment of relative brain iron concentrations using T_2 -weighted and T_2^* -weighted MRI at 3 tesla. *Magnet Reson Med*. 1994;32:335-341. doi:<https://doi.org/10.1002/mrm.1910320309>
4. Reichenbach JR, Venkatesan R, Schillinger DJ, Kido DK, Haacke EM. Small vessels in the human brain: MR venography with deoxyhemoglobin as an intrinsic contrast agent. *Radiology*. 1997;204:272-277. doi:<https://doi.org/10.1148/radiology.204.1.9205259>
5. de Rochefort L, Brown R, Prince MR, Wang Y. Quantitative MR susceptibility mapping using piecewise constant regularized inversion of the magnetic field. *Magnet Reson Med*. 2008;60:1003-1009. doi:<https://doi.org/10.1002/mrm.21710>
6. Wolff SD, Balaban RS. Magnetization transfer contrast (MTC) and tissue water proton relaxation *in vivo*. *Magnet Reson Med*. 1989;10:135-144. doi:<https://doi.org/10.1002/mrm.1910100113>
7. Koenig SH, Brown III RD, Spiller M, Lundbom N. Relaxometry of brain: Why white matter appears bright in MRI. *Magnet Reson Med*. 1990;14:482-495. doi:<https://doi.org/10.1002/mrm.1910140306>
8. Mackay A, Whittall K, Adler J, Li D, Paty D, Graeb D. *In vivo* visualization of myelin water in brain by magnetic resonance. *Magnet Reson Med*. 1994;31:673-677. doi:<https://doi.org/10.1002/mrm.1910310614>
9. Schweser F, Deistung A, Lehr BW, Reichenbach JR. Quantitative imaging of intrinsic magnetic tissue properties using MRI signal phase: An approach to *in vivo* brain iron metabolism? *NeuroImage*. 2011;54:2789-2807. doi:<https://doi.org/10.1016/j.neuroimage.2010.10.070>
10. Fukunaga M, Li T-Q, van Gelderen P, et al. Layer-specific variation of iron content in cerebral cortex as a source of MRI contrast. *P Natl Acad Sci USA*. 2010;107:3834-3839. doi:<https://doi.org/10.1073/pnas.0911177107>
11. Liu C, Li W, Johnson GA, Wu B. High-field (9.4 T) MRI of brain dysmyelination by quantitative mapping of magnetic susceptibility. *NeuroImage*. 2011;56:930-938. doi:<https://doi.org/10.1016/j.neuroimage.2011.02.024>
12. Lee J, Shmueli K, Kang B-T, et al. The contribution of myelin to magnetic susceptibility-weighted contrasts in high-field MRI of the brain. *NeuroImage*. 2012;59:3967-3975. doi:<https://doi.org/10.1016/j.neuroimage.2011.10.076>
13. Shin H-G, Lee J, Yun YH, et al. χ -separation: Magnetic susceptibility source separation toward iron and myelin mapping in the brain. *NeuroImage*. 2021;240:118371. doi:<https://doi.org/10.1016/j.neuroimage.2021.118371>
14. Zhang Z, Cho J, Wang L, et al. Blip up-down acquisition for spin- and gradient-echo imaging (BUDA-SAGE) with self-supervised denoising enables efficient T_2 , T_2^* , para- and dia-magnetic susceptibility mapping. *Magnet Reson Med*. 2022;88:633-650. doi:<https://doi.org/10.1002/mrm.29219>
15. Lee S, Shin H-G, Kim M, Lee J. Depth-wise profiles of iron and myelin in the cortex and white matter using χ -separation: A preliminary study. *NeuroImage*. 2023;273:120058. doi:<https://doi.org/10.1016/j.neuroimage.2023.120058>
16. Lee J, Ji S, Oh S-H. So you want to image myelin using MRI: Advanced magnetic susceptibility imaging for myelin. *arXiv preprint*. 2024;arXiv:2401.03690. doi:<https://doi.org/10.48550/arXiv.2401.03690>
17. Emmerich J, Bachert P, Ladd ME, Straub S. On the separation of susceptibility sources in quantitative susceptibility mapping: Theory and phantom validation with an *in vivo* application to multiple sclerosis lesions of different age. *Journal of Magnetic Resonance*. 2021;330:107033. doi:<https://doi.org/10.1016/j.jmr.2021.107033>
18. Kim W, Shin H-G, Lee H, et al. χ -separation imaging for diagnosis of multiple sclerosis versus neuromyelitis optica spectrum disorder. *Radiology*. 2023;307:e220941. doi:<https://doi.org/10.1148/radiol.220941>
19. Straub S, El-Sanousy E, Emmerich J, Sandig FL, Ladd ME, Schlemmer H-P. Quantitative magnetic resonance imaging biomarkers for cortical pathology in multiple sclerosis at 7 T. *NMR in Biomedicine*. 2023;36(3):e4847. doi:<https://doi.org/10.1002/nbm.4847>
20. Zhu Z, Naji N, Esfahani JH, et al. MR susceptibility separation for quantifying lesion paramagnetic and diamagnetic evolution in relapsing-remitting multiple sclerosis. *Journal of Magnetic Resonance Imaging*. 2024;doi:<https://doi.org/10.1002/jmri.29266>
21. Chen J, Gong N-J, Chaim KT, Otaduy MCG, Liu C. Decompose quantitative susceptibility mapping (QSM) to sub-voxel diamagnetic and paramagnetic components based on gradient-echo MRI data. *NeuroImage*. 2021;242:118477. doi:<https://doi.org/10.1016/j.neuroimage.2021.118477>

22. Dimov AV, Nguyen TD, Gillen KM, et al. Susceptibility source separation from gradient echo data using magnitude decay modeling. *Journal of Neuroimaging*. 2022;32:852-859. doi:<https://doi.org/10.1111/jon.13014>
23. Li Z, Feng R, Liu Q, et al. APART-QSM: An improved sub-voxel quantitative susceptibility mapping for susceptibility source separation using an iterative data fitting method. *NeuroImage*. 2023;274:120148. doi:<https://doi.org/10.1016/j.neuroimage.2023.120148>
24. Evans AC, Janke AL, Collins DL, Baillet S. Brain templates and atlases. *NeuroImage*. 2012;62:911-922. doi:<https://doi.org/10.1016/j.neuroimage.2012.01.024>
25. Lim IAL, Faria AV, Li X, et al. Human brain atlas for automated region of interest selection in quantitative susceptibility mapping: Application to determine iron content in deep gray matter structures. *NeuroImage*. 2013;82:449-469. doi:<https://doi.org/10.1016/j.neuroimage.2013.05.127>
26. Zhang Y, Wei H, Cronin MJ, He N, Yan F, Liu C. Longitudinal atlas for normative human brain development and aging over the lifespan using quantitative susceptibility mapping. *NeuroImage*. 2018;171:176-189. doi:<https://doi.org/10.1016/j.neuroimage.2018.01.008>
27. Li X, Chen L, Kuttan K, et al. Multi-atlas tool for automated segmentation of brain gray matter nuclei and quantification of their magnetic susceptibility. *NeuroImage*. 2019;191:337-349. doi:<https://doi.org/10.1016/j.neuroimage.2019.02.016>
28. Liu H, Rubino C, Dvorak AV, et al. Myelin water atlas: A template for myelin distribution in the brain. *Journal of Neuroimaging*. 2019;29(6):699-706. doi:<https://doi.org/10.1111/jon.12657>
29. Dvorak AV, Swift-LaPointe T, Vavasour IM, et al. An atlas for human brain myelin content throughout the adult life span. *Scientific Reports*. 2021;11:269. doi:<https://doi.org/10.1038/s41598-020-79540-3>
30. Lao G, Liu Q, Li Z, et al. Sub-voxel quantitative susceptibility mapping for assessing whole-brain magnetic susceptibility from ages 4 to 80. *Human Brain Mapping*. 2023;44:5953-5971. doi:<https://doi.org/10.1002/hbm.26487>
31. Tustison NJ, Avants BB, Cook PA, et al. N4ITK: Improved N3 bias correction. *IEEE Transactions on Medical Imaging*. 2010;29(6):1310-1320. doi:<https://doi.org/10.1109/TMI.2010.2046908>
32. Kim M, Shin H-G, Oh C, et al. Chi-sepnet: Susceptibility source separation using deep neural network. *Proceedings of International Society of Magnetic Resonance in Medicine*. 2022;30:2464.
33. Shin H-G, Seo J, Lee Y, et al. Chi-separation using multi-orientation data in *in vivo* and *ex vivo* brains: Visualization of histology up to the resolution of 350 μm . *Proceedings of International Society of Magnetic Resonance in Medicine*. 2022;30:0771.
34. Jang J, Shin H-G, Kim M, Lee H, Kim W. Comparison of chi-separation and chi-separation*: A clinical feasibility study. *Proceedings of International Society of Magnetic Resonance in Medicine*. 2023;31:2826.
35. Schofield MA, Zhu Y. Fast phase unwrapping algorithm for interferometric applications. *Optics Letters*. 2003;28(14):1194-1196. doi:<https://doi.org/10.1364/OL.28.001194>
36. Wu B, Li W, Avram AV, Gho S-M, Liu C. Fast and tissue-optimized mapping of magnetic susceptibility and T2* with multi-echo and multi-shot spirals. *NeuroImage*. 2012;59:297-305. doi:<https://doi.org/10.1016/j.neuroimage.2011.07.019>
37. Wu B, Li W, Guidon A, Liu C. Whole brain susceptibility mapping using compressed sensing. *Magnet Reson Med*. 2012;67:137-147. doi:<https://doi.org/10.1002/mrm.23000>
38. Hanspach J, Dwyer MG, Bergsland NP, et al. Methods for the computation of templates from quantitative magnetic susceptibility maps (QSM): Toward improved atlas- and voxel-based analyses (VBA). *Journal of Magnetic Resonance Imaging*. 2017;46:1474-1484. doi:<https://doi.org/10.1002/jmri.25671>
39. He C, Guan X, Zhang W, et al. Quantitative susceptibility atlas construction in Montreal Neurological Institute space: Towards histological-consistent iron-rich deep brain nucleus subregion identification. *Brain Structure and Function*. 2023;228:1045-1067. doi:<https://doi.org/10.1007/s00429-022-02547-1>
40. Nyúl LG, Udupa JK, Zhang X. New variants of a method of MRI scale standardization. *IEEE Transactions on Medical Imaging*. 2000;19(2):143-150. doi:<https://doi.org/10.1109/42.836373>
41. Avants BB, Epstein CL, Grossman M, Gee JC. Symmetric diffeomorphic image registration with cross-correlation: Evaluating automated labeling of elderly and neurodegenerative brain. *Medical Image Analysis*. 2008;12:26-41. doi:<https://doi.org/10.1016/j.media.2007.06.004>
42. Mori S, Wakana S, Nagae-Poetscher LM, van Zijl PCM. *MRI Atlas of Human White Matter*. Elsevier; 2005.
43. Avants BB, Tustison NJ, Wu J, Cook PA, Gee JC. An open source multivariate framework for *n*-tissue segmentation with evaluation on public data. *Neuroinformatics*. 2011;9:381-400. doi:<https://doi.org/10.1007/s12021-011-9109-y>
44. Hallgren B, Sourander P. The effect of age on the non-haemin iron in the human brain. *Journal of Neurochemistry*. 1958;3:41-51. doi:<https://doi.org/10.1111/j.1471-4159.1958.tb12607.x>
45. Langkammer C, Schweser F, Krebs N, et al. Quantitative susceptibility mapping (QSM) as a means to measure brain iron? A post mortem validation study. *NeuroImage*. 2012;62:1593-1599. doi:<https://doi.org/10.1016/j.neuroimage.2012.05.049>

46. Naidich TP, Castillo M, Cha S, Smirniotopoulos JG. *Imaging of the Brain*. 1st ed. Saunders; 2013.
47. Schaltenbrand G, Wahren W. *Atlas for Stereotaxy of the Human Brain*. 2nd ed. Thieme; 1977.
48. Faizy TD, Kumar D, Broocks G, et al. Age-related measurements of the myelin water fraction derived from 3D multi-echo GRASE reflect myelin content of the cerebral white matter. *Scientific Reports*. 2018;8:14991.
49. Papadaki E, Kavroulakis E, Kalaitzakis G, et al. Age-related deep white matter changes in myelin and water content: A T₂ relaxometry study. *Journal of Magnetic Resonance Imaging*. 2019;50:1393-1404.
50. Faizy TD, Thaler C, Broocks G, et al. The myelin water fraction serves as a marker for age-related myelin alterations in the cerebral white matter - A multiparametric MRI aging study. *Frontiers in Neuroscience*. 2020;14:136.
51. Lee J, Shmueli K, Fukunaga M, et al. Sensitivity of MRI resonance frequency to the orientation of brain tissue microstructure. *P Natl Acad Sci USA*. 2010;107:5130-5135. doi:<https://doi.org/10.1073/pnas.0910222107>
52. Wharton S, Bowtell R. Effects of white matter microstructure on phase and susceptibility maps. *Magnet Reson Med*. 2015;73:1258-1269. doi:<https://doi.org/10.1002/mrm.25189>
53. Lee J, van Gelderen P, Kuo L-W, Merkle H, Silva AC, Duyn JH. T₂*-based fiber orientation mapping. *NeuroImage*. 2011;57:225-234. doi:<https://doi.org/10.1016/j.neuroimage.2011.04.026>
54. Lee J, Shin H-G, Jung W, Nam Y, Oh S-H, Lee J. An R₂* model of white matter for fiber orientation and myelin concentration. *NeuroImage*. 2017;162:269-275. doi:<https://doi.org/10.1016/j.neuroimage.2017.08.050>
55. Grosso E, Ricciardi A, D'Angelo E, Palesi F, Wheeler-Kingshott CAG. Subject-specific χ -separation method: The effect of introducing a personalised relaxometric constant D_r. *Proceedings of International Society of Magnetic Resonance in Medicine*. 2022;30:4172.
56. Lebel C, Beaulieu C. Longitudinal development of human brain wiring continues from childhood into adulthood. *J Neurosci*. 2011;31(30):10937-10947. doi:<https://doi.org/10.1523/jneurosci.5302-10.2011>
57. Bilgic B, Pfefferbaum A, Rohlfing T, Sullivan EV, Adalsteinsson E. MRI estimates of brain iron concentration in normal aging using quantitative susceptibility mapping. *NeuroImage*. 2012;59:2625-2635.
58. Li W, Wu B, Batrachenko A, et al. Differential developmental trajectories of magnetic susceptibility in human brain gray and white matter over the lifespan. *Human Brain Mapping*. 2014;35:2698-2713. doi:<https://doi.org/10.1002/hbm.22360>
59. Li W, Langkammer C, Chou Y-H, et al. Association between increased magnetic susceptibility of deep gray matter nuclei and decreased motor function in healthy adults. *NeuroImage*. 2015;105:45-52. doi:<https://doi.org/10.1016/j.neuroimage.2014.10.009>
60. van Bergen JMG, Li X, Quevenno FC, et al. Low cortical iron and high entorhinal cortex volume promote cognitive functioning in the oldest-old. *Neurobiology of Aging*. 2018;64:68-75. doi:<https://doi.org/10.1016/j.neurobiolaging.2017.12.014>
61. Wang Q, Xu X, Zhang M. Normal aging in the basal ganglia evaluated by eigenvalues of diffusion tensor imaging. *Am J Neuroradiol*. 2010;31:516-520. doi:<https://doi.org/10.3174/ajnr.a1862>
62. Cherubini A, Péran P, Caltagirone C, Sabatini U, Spalletta G. Aging of subcortical nuclei: Microstructural, mineralization and atrophy modifications measured in vivo using MRI. *NeuroImage*. 2009;48:29-36. doi:<https://doi.org/10.1016/j.neuroimage.2009.06.035>
63. Arshad M, Stanley JA, Raz N. Adult age differences in subcortical myelin content are consistent with protracted myelination and unrelated to diffusion tensor imaging indices. *NeuroImage*. 2016;143:26-39.
64. Hebbrecht G, Maenhaut W, De Reuck J. Brain trace elements and aging. *Nuclear Instruments and Methods in Physics Research B*. 1999;150:208-213. doi:[https://doi.org/10.1016/S0168-583X\(98\)00938-0](https://doi.org/10.1016/S0168-583X(98)00938-0)
65. Pyatigorskaya N, Sanz-Morère CB, Gaurav R, et al. Iron imaging as a diagnostic tool for Parkinson's disease: A systematic review and meta-analysis. *Frontiers in Neurology*. 2020;11:366. doi:<https://doi.org/10.3389/fneur.2020.00366>
66. Jang J, Nam Y, Jung SW, Riew T-R, Kim SH, Kim I-B. Paradoxical paramagnetic calcifications in the globus pallidus: An ex vivo MR investigation and histological validation study. *NMR in Biomedicine*. 2021;34:e4571. doi:<https://doi.org/10.1002/nbm.4571>
67. Lozano AM, Lipsman N, Bergman H, et al. Deep brain stimulation: Current challenges and future directions. *Nature Reviews Neurology*. 2019;15:146-160. doi:<https://doi.org/10.1038/s41582-018-0128-2>
68. Chang KW, Jung HH, Chang JW. Magnetic resonance-guided focused ultrasound surgery for obsessive-compulsive disorders: Potential for use as a novel ablative surgical technique. *Frontiers in Psychiatry*. 2021;12:640832. doi:<https://doi.org/10.3389/fpsy.2021.640832>

Supplementary information for

A human brain atlas of χ -separation for normative iron and myelin distributions

Kyeongseon Min, Beomseok Sohn, Woo Jung Kim, Chae Jung Park, Soohwa Song, Dong Hoon Shin, Kyung Won Chang, Na-Young Shin, Minjun Kim, Hyeong-Geol Shin, Phil Hyu Lee, Jongho Lee*

Table of contents

Supplementary methods

- Recruitment criteria for healthy volunteers
- Magnetization-prepared rapid gradient echo (MPRAGE) scan parameters

Supplementary figures

- Figures S1–S2

Supplementary tables

- Tables S1–S2

Supplementary methods

Recruitment criteria for healthy volunteers

80 healthy volunteers from Yonsei Severance Hospital (YSSH) and 12 from Yongin Severance Hospital (YGSH) were recruited based on the following criteria: individuals with no history of major neurological disorders or mental disorders, no family history of movement disorders, a cross-cultural smell identification test score of 8 or higher, and a mini-mental state examination score of 27 or higher. Additionally, 24 healthy volunteers were recruited from YGSH with the following criteria: individuals with no history of major neurological disorders or mental disorders, no evidence of severe or unstable physical conditions, no history of substance use disorders within the last 3 years, individuals determined to be normal in an activities of daily living evaluation, individuals determined to be normal in a subjective cognitive decline survey, and individuals who showed normal performance in all cognitive areas in a neuropsychological test.

Magnetization-prepared rapid gradient echo (MPRAGE) scan parameters

T_1 -weighted images were acquired from 116 subjects using 3D MPRAGE sequences. Scan parameters varied as follows: TR = 9.8 ms, TE = 4.6 ms, flip angle = 8° for 80 subjects from YSSH; TR = 7.2 ms, TE = 3.3 ms, flip angle = 9° for 12 subjects from YGSH; and TR = 4.6 ms, TE = 2.0 ms, flip angle = 8° for 24 subjects from YGSH. All had a resolution of $1 \times 1 \times 1 \text{ mm}^3$ and an FOV of $240 \times 190 \times 240 \text{ mm}^3$. The FOV was adjusted to reduce scan time.

Supplementary figures

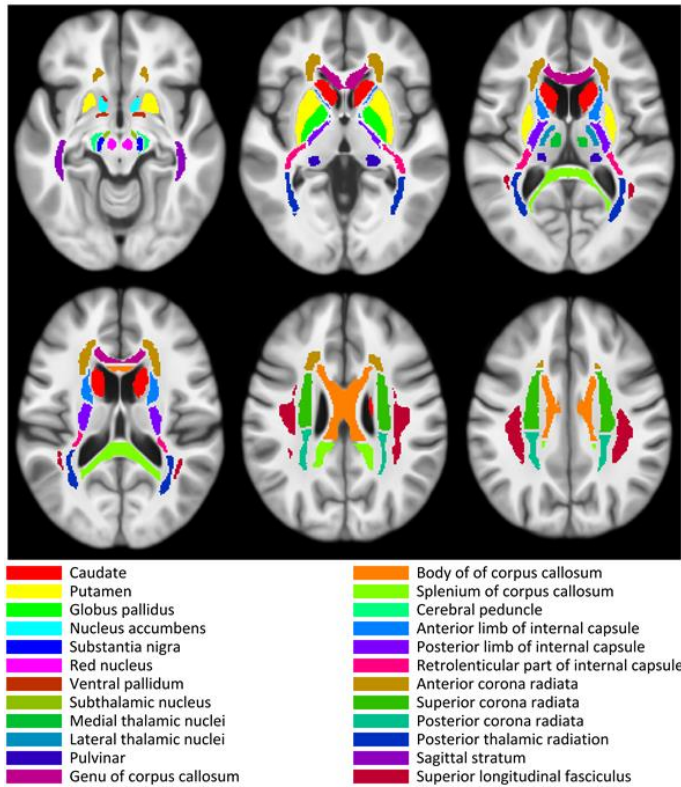


Fig. S1. The regions of interests (ROI) used for the analysis are overlaid on T_1 -weighted axial slices. The corresponding color codes are presented below. The ROI labels are publicly available (<https://github.com/SNU-LIST/chi-separation-atlas>).

Artifacts in χ -separation atlas

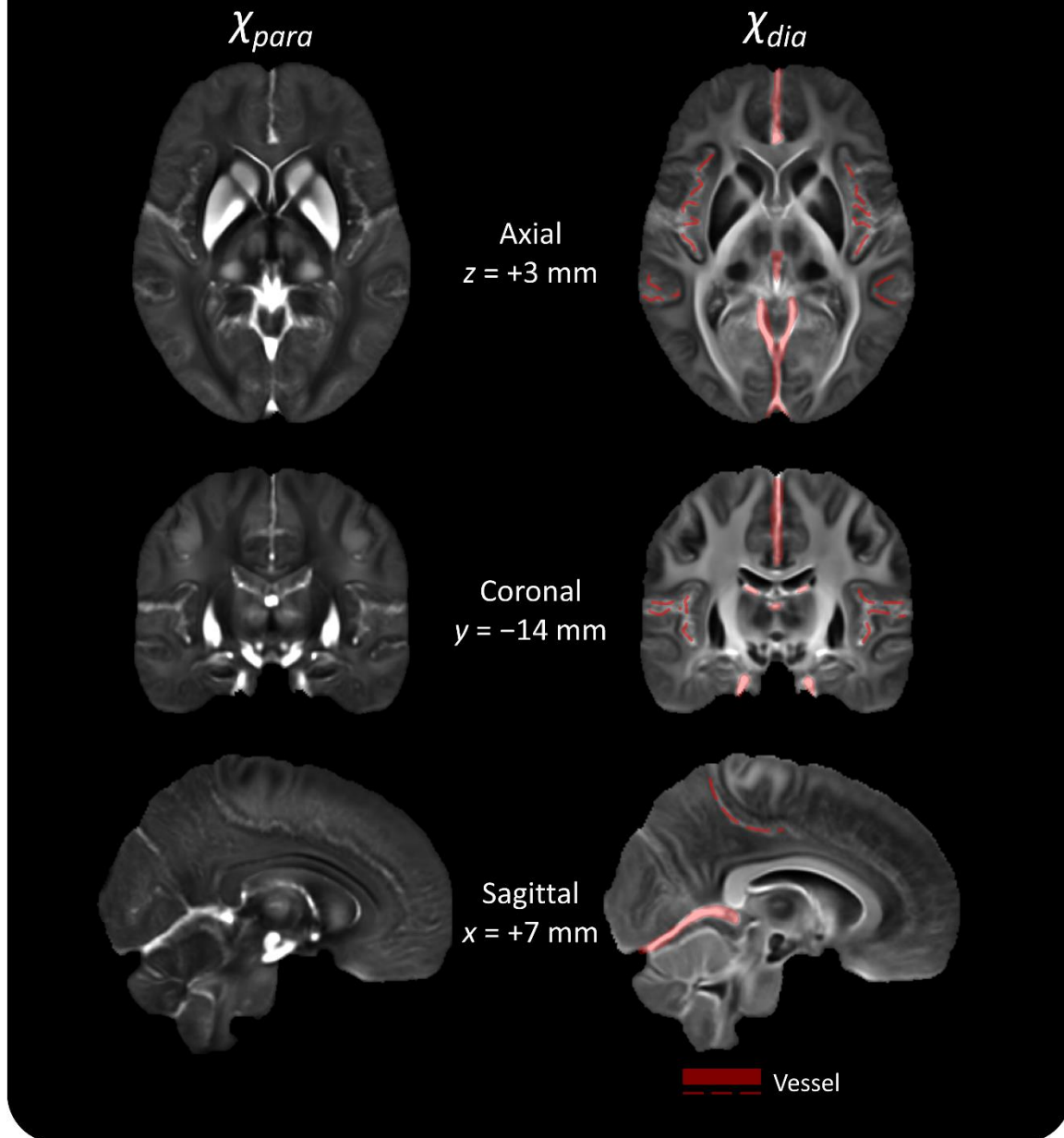


Fig. S2. Artifacts in χ -separation atlas. Vessel artifacts in the χ_{dia} atlas are marked with red overlay.

Supplementary tables

Table S1. Population means and standard deviations of χ_{para} and χ_{dia} values in subcortical nuclei, thalamic nuclei, and white matter ROIs.

	ROI name	χ_{para} (ppb)	χ_{dia} (ppb)
Subcortical nuclei	Caudate	47.7 ± 7.4	-8.2 ± 4.9
	Putamen	77.1 ± 20.6	-10.3 ± 5.9
	Globus pallidus	131.9 ± 10.4	-12.6 ± 7.3
	Nucleus accumbens	45.4 ± 13.2	-23.4 ± 5.6
	Substantia nigra	115.7 ± 14.4	-11.1 ± 4.5
	Red nucleus	112.0 ± 14.8	-10.1 ± 4.1
	Ventral pallidum	144.3 ± 27.0	-22.1 ± 13.1
	Subthalamic nucleus	112.1 ± 12.1	-15.3 ± 5.9
	Thalamus	Medial thalamic nuclei	31.2 ± 7.6
Lateral thalamic nuclei		22.0 ± 5.2	-22.4 ± 4.7
Pulvinar		52.1 ± 11.6	-4.4 ± 3.2
Whole thalamus		22.9 ± 2.1	-20.8 ± 2.5
White matter	Genu of corpus callosum	17.8 ± 1.9	-30.8 ± 2.9
	Body of corpus callosum	14.8 ± 1.9	-35.1 ± 2.6
	Splenium of corpus callosum	16.5 ± 2.6	-42.3 ± 3.1
	Cerebral peduncle	23.5 ± 2.8	-43.7 ± 4.1
	Anterior limb of internal capsule	14.5 ± 2.2	-41.3 ± 4.0
	Posterior limb of internal capsule	8.2 ± 2.7	-52.2 ± 3.0
	Retrolenticular part of internal capsule	18.0 ± 2.9	-39.3 ± 3.3
	Anterior corona radiata	13.9 ± 1.7	-27.1 ± 2.9
	Superior corona radiata	14.1 ± 1.6	-31.7 ± 2.9
	Posterior corona radiata	14.0 ± 2.3	-32.0 ± 2.5
	Posterior thalamic radiation	12.9 ± 2.5	-41.1 ± 4.0
	Sagittal stratum	17.3 ± 2.2	-36.5 ± 3.9
	Superior longitudinal fasciculus	22.6 ± 1.6	-32.7 ± 2.9
Whole white matter	16.8 ± 1.1	-28.8 ± 1.9	

Table S2. Age-dependence of χ_{para} and χ_{dia} values in subcortical nuclei, thalamic nuclei, and white matter ROIs. The χ_{para} and χ_{dia} values were regressed with a linear function of age. Regression coefficients with statistical significance are marked with asterisks (*, $p < 0.05$, Bonferroni-corrected).

$$\chi_{para} \text{ or } |\chi_{dia}| \text{ (ppb)} = [\text{Slope (ppb/years)}] \times (\text{age} - 60) \text{ (years)} + [\text{Intercept (ppb)}].$$

	ROI name	χ_{para} (ppb)		$ \chi_{dia} $ (ppb)	
		Slope	Intercept	Slope	Intercept
Subcortical nuclei	Caudate	0.08	47.59*	0.19*	8.05*
	Putamen	0.85*	76.40*	0.15*	10.16*
	Globus pallidus	0.08	131.84*	0.21*	12.43*
	Nucleus accumbens	0.59*	44.87*	0.15*	23.25*
	Substantia nigra	0.07	115.62*	0.01	11.13*
	Red nucleus	0.07	111.91*	0.00	10.13*
	Ventral pallidum	0.38	143.96*	0.32*	21.87*
	Subthalamic nucleus	0.04	112.04*	0.06	15.21*
Thalamus	Medial thalamic nuclei	-0.20*	31.37*	0.05	11.79*
	Lateral thalamic nuclei	-0.17*	22.12*	-0.02	22.40*
	Pulvinar	-0.10	52.21*	-0.01	4.41*
	Whole thalamus	-0.14*	22.98*	0.00	20.78*
White matter	Genu of corpus callosum	0.03	17.80*	0.01	30.79*
	Body of corpus callosum	-0.05*	14.51*	0.00	35.10*
	Splenium of corpus callosum	-0.04	16.54*	-0.09*	42.40*
	Cerebral peduncle	-0.04	23.51*	-0.01	43.68*
	Anterior limb of internal capsule	0.01	14.51*	-0.14*	41.43*
	Posterior limb of internal capsule	-0.07*	8.29*	-0.08*	52.23*
	Retrolenticular part of internal capsule	-0.06	18.07*	-0.12*	39.45*
	Anterior corona radiata	-0.01	13.90*	-0.10*	27.18*
	Superior corona radiata	-0.04*	14.17*	-0.07*	31.72*
	Posterior corona radiata	-0.08*	14.03*	-0.03	32.01*
	Posterior thalamic radiation	-0.10*	12.95*	-0.05	41.09*
	Sagittal stratum	-0.01	17.26*	-0.05	36.54*
	Superior longitudinal fasciculus	-0.01	22.56*	-0.06*	32.72*
	Whole white matter	-0.02	16.82*	-0.05*	28.81*